
Please note that this is a preprint listed on EarthArXiv which has not undergone full peer review yet. Subsequent versions may have slightly different content. If accepted, the final version of this manuscript will be available via the ‘Peer-reviewed Publication DOI’ link on the right-hand side of this webpage. Please feel free to contact any of the authors; we welcome the feedback.

Rapid fault healing after seismic slip

John D. Bedford^{1,2*}, Takehiro Hirose¹ and Yohei Hamada¹

¹Kochi Institute for Core Sample Research (X-star), Japan Agency for Marine-Earth Science and Technology (JAMSTEC), 200 Monobe-otsu, Nankoku, Kochi 783-8502, Japan

²Now at Department of Earth, Ocean and Ecological Sciences, University of Liverpool, Liverpool, L69 3GP, UK

*Corresponding author: John Bedford (jbedford@liverpool.ac.uk)

Highlights

- We investigate fault healing behavior of gabbro and granite gouges after they have experienced dynamic weakening during high-velocity slip
- Once slip has ceased, the fault gouges rapidly recover the strength they lost during the high-velocity slip events
- Enhanced healing is likely caused by thermally activated chemical bonding at asperity contacts in the gouge

16 **Abstract**

17 Fault strength recovery (healing) following an earthquake is a key process in controlling the recurrence of
18 future events; however, the rates and mechanisms of fault healing are poorly constrained. Here, by
19 performing high-velocity friction experiments at seismic slip rates (0.57 m/s), we show that granite and
20 gabbro fault gouges recover their strength rapidly after experiencing dynamic weakening. The healing rates
21 are two orders of magnitude faster than those observed in typical frictional healing experiments performed
22 at slow slip velocities (micrometers to millimeters per second). Analysis of the sheared gouges using Raman
23 spectroscopy suggests that enhanced healing after seismic slip is associated with thermally activated
24 chemical bonding at frictional contacts in the gouge. Our results imply that seismogenic faults regain their
25 strength early during interseismic periods, indicating that healing may not be the dominant control on
26 earthquake recurrence, with other processes, such as far-field tectonic loading or frictional stability
27 transitions, likely dictating the occurrence of future events.

28

29 **Plain Language Summary**

30 During an earthquake, faults experience a dynamic reduction in their frictional strength due to processes
31 such as shear heating. How quickly faults can regain their strength (i.e., heal) after an earthquake is
32 important for controlling when future events might occur. Here, we perform high-velocity shearing
33 experiments on simulated faults – at similar slip speeds that natural faults slide at during real earthquakes -
34 to investigate how faults weaken and then subsequently recover their strength during and after a seismic
35 event. We find that our experimental faults recover they strength rapidly after a seismic slip event, with the
36 rate of strength recovery being two orders of magnitude faster than healing rates typically observed in
37 traditional frictional healing experiments performed at much slower sliding velocities. We perform
38 chemical analyses on our sheared faults and find a change in the chemical bonding properties of the fault
39 surface after a simulated earthquake event. We therefore hypothesize that the rapid fault restrengthening
40 we observe once the fault has stopped slipping is caused by enhanced chemical bonding at frictional

41 contacts along the experimental faults. Our results suggest that natural tectonic faults will recover their
42 strength quickly after an earthquake has occurred.

43

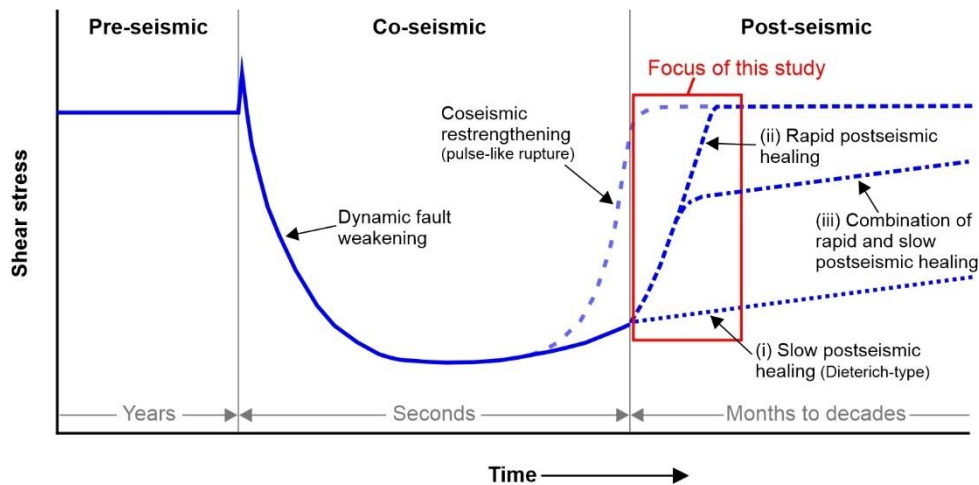
44 **1. Introduction**

45 Faults slip suddenly during earthquakes, accelerating to velocities on the order of a few meters per
46 second. At these seismic slip velocities a significant reduction in fault strength occurs (Di Toro et al., 2011)
47 as a result of various dynamic weakening mechanisms becoming activated by shear heating and/or grain
48 size reductions (Tullis, 2015). Although our knowledge of dynamic fault weakening processes has increased
49 significantly over the last 25 years since the advent of high-velocity friction experiments (Tsutsumi &
50 Shimamoto, 1997), our understanding of how faults regain their strength after dynamic weakening, once
51 seismic slip has ceased, is more limited. Fault restrengthening is a fundamental process in the earthquake
52 cycle that may control the recurrence time (Vidale et al., 1994), the mode of slip (Shreedharan et al., 2023),
53 the maximum strength that can be attained (Kanamori & Allen, 1986; Scholz et al., 1986), and the nature
54 of radiated energy (McLaskey et al., 2012) in future events.

55 The rate of fault restrengthening can vary with both time and space along the fault during the earthquake
56 cycle (Li et al., 2006; Pei et al., 2019). Restrengthening may occur initially during coseismic slip itself, as
57 sometimes observed during the deceleration phase of high-velocity friction experiments (Harbord et al.,
58 2021; Proctor et al., 2014; Sone & Shimamoto, 2009; Violay et al., 2019). Coseismic restrengthening (Fig.
59 1) is a potentially important process in the generation of pulse-like earthquake ruptures (Heaton, 1990),
60 which require that faults rapidly regain their strength (self-heal) after the passage of the rupture front.
61 However, the mechanisms of coseismic restrengthening are poorly constrained and it is a phenomenon that
62 is not always observed in experiments, or it may only partially recover the strength lost during high-velocity
63 fault slip (Boulton et al., 2017; Han et al., 2007; Hunfeld et al., 2021; Seyler et al., 2020; Yao et al., 2013).
64 In such cases, the majority of fault restrengthening must occur in the postseismic regime instead, when the
65 fault is held in quasi-stationary contact.

66 The process of strength recovery as a fault is held in quasi-stationary contact, known as fault healing,
 67 has been extensively studied in experiments performed at slow sliding velocities, on the order of
 68 micrometers per second (Marone & Saffer, 2015). The common procedure for studying fault healing in the
 69 laboratory is to perform slide-hold-slide (SHS) experiments (Dieterich, 1972; Marone, 1997), whereby the
 70 shearing of fault materials is paused for predetermined durations and then shear strength is monitored as
 71 sliding is resumed after the hold period. Previous low-velocity SHS experiments have shown that frictional
 72 strength typically increases linearly with the logarithm of hold time, with healing rate being dependent on
 73 the composition of the fault materials (Carpenter et al., 2016); although it should be noted that some
 74 materials (e.g., clays) have been reported to display a negative or near-zero change in frictional strength
 75 with hold time (e.g., Orellana et al., 2018; Shreedharan et al., 2023). The physical mechanisms responsible
 76 for fault healing are debated, with time-dependent growth of real contact area due to asperity creep often
 77 invoked to explain healing behavior (Dieterich & Kilgore, 1994). However, more recent work has suggested
 78 other processes such as chemical bond formation could be responsible for fault healing observed in
 79 laboratory experiments (Li et al., 2011; Thom et al., 2018).

80



81

82 **Figure 1:** Schematic diagram of fault strength evolution during the seismic cycle. During coseismic slip, a
 83 significant reduction in shear stress occurs as a result of dynamic fault weakening. In the postseismic

84 *regime the fault regains its strength as it is held in quasi-stationary contact. The aim of this study is to*
85 *determine whether fault strength recovery immediately following seismic slip occurs via (i) slow*
86 *“Dieterich-type” healing, (ii) rapid postseismic healing, or (iii) a combination of rapid and slow healing.*

87

88 In some specific cases, the healing rates determined from low-velocity SHS experiments correlate well
89 with stress drops observed during sequences of small repeating earthquakes in nature (i.e., the magnitude
90 of the stress drop increases as the duration of the recurrence interval increases (Marone et al., 1995; Vidale
91 et al., 1994)). However, following large earthquakes, geophysical observations suggest that rapid fault
92 restrengthening can occur in comparison to typical recurrence intervals, with the majority of the strength
93 being recovered early during the interseismic period. For example, shear-wave splitting measurements
94 following the 1995 Kobe earthquake (moment magnitude M_w 6.9) on the Nojima fault indicate that the
95 majority of fault strength had recovered within 33 months of the main event (recurrence interval of
96 approximately 2000 years) (Tadokoro & Ando, 2002). Borehole permeability measurements from the
97 Longmenshan fault zone that hosted the 2008 Wenchuan earthquake (M_w 7.9), suggest that the fault healed
98 within 0.6 to 2.5 years after the earthquake (Xue et al., 2013). Seismic velocity measurements made
99 following the same event, and also the nearby 2013 Lushan earthquake (M_w 6.6), support the notion of rapid
100 healing on the fault (Pei et al., 2019), with similar enhanced strength recovery rates also inferred after the
101 2004 Parkfield earthquake (M_w 6.0) on the San Andreas fault (Y.-G. Li et al., 2006) and between the 2019
102 Ridgecrest earthquake pair (M_w 6.4 and M_w 7.1) in the eastern California shear zone (Magen et al., 2020).
103 Geophysical observations thus potentially indicate that different postseismic healing processes are in
104 operation immediately following large earthquakes, leading to more rapid restrengthening, than the classic
105 “Dieterich-type” healing mechanisms (Dieterich, 1972; Dieterich & Kilgore, 1994) responsible for fault
106 strengthening in low-velocity SHS experiments (Fig. 1). It should also be noted that over typical recurrence
107 intervals of large earthquakes (up to several hundreds of years), processes such as cementation and pressure
108 solution will increase cohesion of fault materials, contributing to the long-term strength evolution of the

109 fault during interseismic periods (van den Ende & Niemeijer, 2019; Muhuri et al., 2003; Tenthorey & Cox,
110 2006).

111 In order to investigate rapid postseismic healing processes in the laboratory we need to simulate
112 earthquake slip velocities, something that is not done in typical low-velocity SHS experiments. By shearing
113 at seismic slip velocities, the fault materials will also experience dynamic weakening (Di Toro et al., 2011),
114 which more closely mimics what happens during natural earthquakes. Here, we perform high-velocity (0.57
115 m/s) SHS experiments on gabbro and granite gouges under room humidity conditions at a constant normal
116 stress of 1.5 MPa in all experiments, to investigate how the gouges regain their strength during quasi-
117 stationary hold periods after experiencing dynamic weakening. We varied the duration of the static hold
118 period in order to determine whether the postseismic restrengthening behavior exhibits either, (i)
119 “Dieterich-type” healing as observed in low-velocity SHS experiments, (ii) a form of more rapid healing,
120 or (iii) a combination of rapid and slow healing; as shown schematically in Figure 1. We then analyze the
121 microstructures of the sheared gouges and perform Raman spectroscopy in an attempt elucidate the
122 underlying healing mechanisms in operation after seismic slip events.

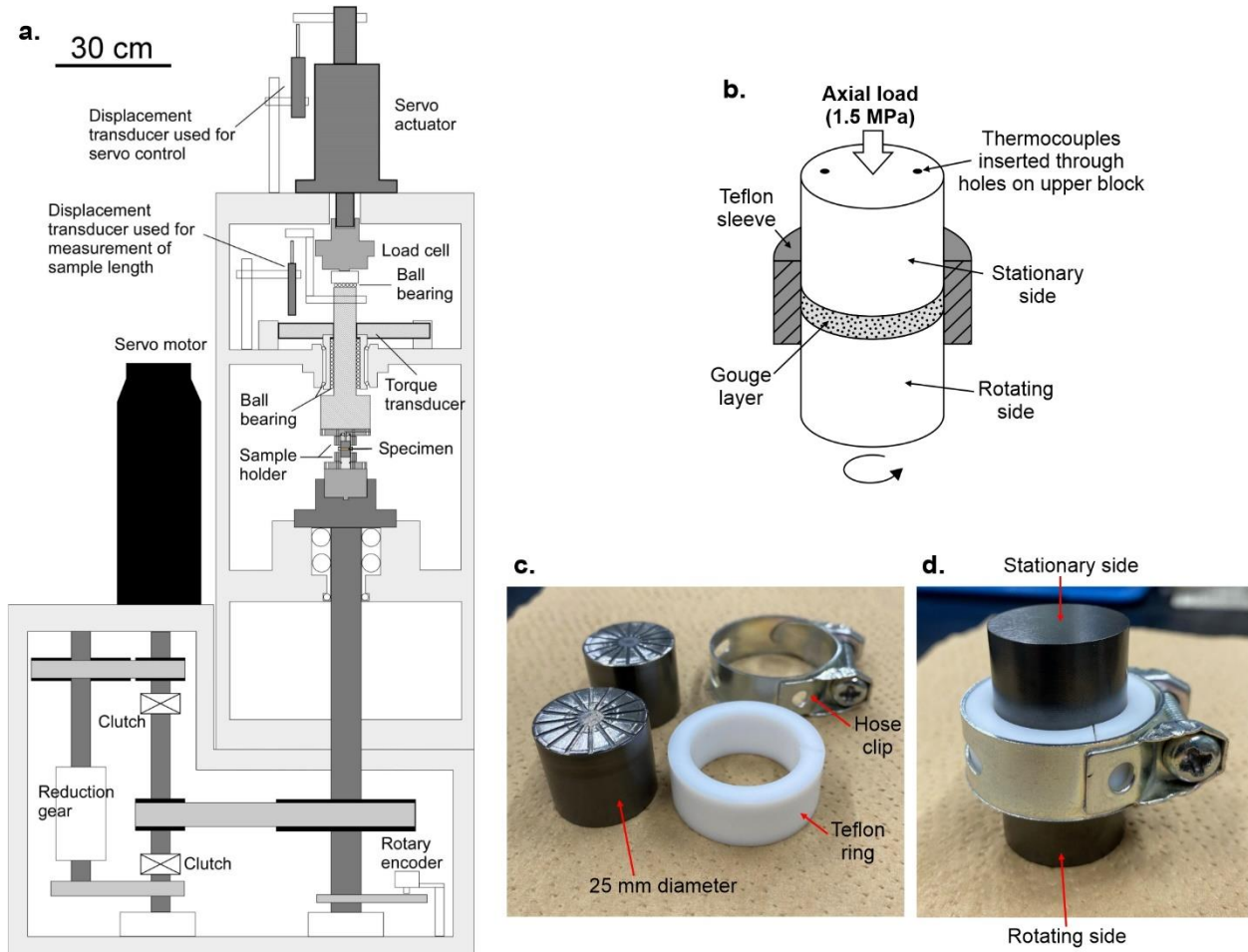
123

124 **2. Methods**

125 ***2.1. Experimental procedure***

126 The experimental samples were produced by crushing and sieving intact samples of Inada granite
127 and Belfast gabbro to form simulated fault gouges (powders) with grain sizes between 63-125 μm . A layer
128 of simulated gouge (measured by weight to produce a layer with an initial thickness of 1.5 mm) was then
129 sandwiched between two cylindrical stainless steel experimental forcing blocks (diameter = 25 mm). The
130 surface of the blocks contains radial grooves (0.5 mm deep) to minimize boundary shear between the gouge
131 layer and the forcing blocks during the experiments. To limit gouge loss during shearing, the gouge layer
132 was contained laterally by a 5 mm thick polytetrafluoroethylene (PTFE) sleeve (Fig. 2b). The low-friction

133 PTFE sleeve was cut and tightened onto the forcing blocks using a hose clip (Fig. 2c-d), following the
 134 procedure outlined in the supplementary material of De Paola et al., (2015). We used a torque-screwdriver
 135 to ensure the hose clip was tightened by the same amount for each experiment. Once the gouge sample was
 136 constructed in between the forcing blocks, it was sheared using the PHV rotary shear apparatus (Fig. 2a) in
 137 the Rock Mechanics Laboratory at the Kochi Institute for Core Sample Research (Japan).



138

139 **Figure 2.** (a) Schematic diagram of the PHV rotary shear apparatus (modified from Tanikawa et al.,
 140 (2012)). (b) Schematic diagram of the experimental sample configuration. The gouge layer is sandwiched
 141 between two cylindrical steel experimental forcing blocks and contained laterally by a Teflon ring. (c)
 142 Photograph of the disassembled components of the sample assembly. (d) Photograph of the assembled
 143 sample setup; the Teflon ring is cut and then tightened on to the assembly using a hose clip.

144

145 Before the main SHS experiment, the gouge samples were pre-sheared for four complete
146 revolutions (equivalent to 0.2 m of slip) under a normal stress of 0.75 MPa at a rate of 1.7 mm/s, to ensure
147 the gouge layer thickness was even across the sample. The normal stress was then increased to the
148 experimental target value of 1.5 MPa. As all experiments were run under the same normal stress we did not
149 correct for the shear stress contribution from the PTFE sleeve, with previous work showing that the
150 mechanical contribution from the PTFE is negligible (Seyler et al., 2020). All tests were conducted under
151 room temperature (22-25 °C) and humidity (30-50%) conditions. As the slip velocity varies with radial
152 position, we use an “equivalent slip velocity” (v_e) which corresponds to the velocity at 2/3 of the radius of
153 the cylindrical specimens (De Paola et al., 2015), given by:

$$154 \quad v_e = \frac{4\pi Rr}{3}$$

155 where R is the revolution rate of the motor and r is the sample radius. In our experiments, the gouge layers
156 were sheared at 0.57 m/s for an equivalent slip displacement (d_e) of 15 m (650 rpm for 285 revolutions)
157 during the first sliding event (slide 1, in Fig. 3), they were then held in quasi-stationary contact for a
158 predetermined amount of time, before being sheared again for another 15 m at 0.57 m/s (slide 2).

159 In some of the high-velocity experiments temperature measurements were made by placing
160 thermocouples next to the upper surface of the gouge layer (<0.5 mm above the gouge surface). Two holes
161 were drilled into the upper experimental forcing block (on the stationary side of the fault, Fig. 2b) and
162 thermocouples were inserted and sealed into place using a ceramic bond. The thermocouples were
163 positioned at 2/3 of the radius so that the temperature measurements were consistent with the calculated v_e
164 and d_e .

165 As well as the high-velocity SHS experiments, some additional tests were performed at
166 micrometer-per-second slip velocities to compare healing rates after low-velocity slip with the rates

167 determined in our high-velocity experiments. In the low-velocity SHS experiments (performed at an
168 equivalent slip velocity of $2.6 \mu\text{m/s}$) we used intact cylindrical rock-to-rock samples of Inada granite and
169 Belfast gabbro, instead of gouge. Initially we tried performing the low-velocity SHS experiments using
170 gouge samples, however, we found negligible healing even after hold periods $>1000 \text{ s}$ (healing rate, $\beta \approx$
171 0). We believe this is due to the low normal stress conditions and also low shear strain the gouge had
172 experienced before the low-velocity SHS experiments were performed. We tried to perform experiments
173 where the gouges were sheared at millimeter-per-second slip velocities to an equivalent slip displacement
174 of 15 m prior to the low-velocity SHS tests (i.e., the same d_e as achieved in the high-velocity SHS
175 experiments), however, there was a large amount of gouge extrusion from between the PTFE ring and the
176 metal forcing blocks during the pre-shearing. Therefore, as the purpose of our low-velocity SHS
177 experiments is just to provide an approximate representation of typical healing rates at slow sliding
178 velocities, we chose to instead include data from rock-to-rock samples in Fig. 4, as the healing rates we
179 determined from the rock-to-rock samples are close to previously reported healing rates observed in many
180 low-velocity friction studies on both gouge and intact rock samples of granite and gabbro (e.g., Beeler et
181 al., 1994; Carpenter et al., 2016; Giacomel et al., 2021; Mitchell et al., 2013). Prior to the low-velocity SHS
182 experiments, the cylindrical rock samples were rotated for more than 1000 rotations at a constant speed of
183 4 rpm ($v_e = 3.5 \text{ mm/s}$) over a range of incrementally increasing normal stresses from 0.3 to 1.4 MPa . The
184 purpose of this procedure was to remove any heterogeneities and ensure the surfaces on opposite side of
185 the sliding interface were parallel. The wear materials produced on the sliding surface during this pre-
186 sliding were not removed before the SHS experiments, thus the rock samples were separated by a thin
187 gouge layer during the experiments. The wear materials produced during the experiments were allowed to
188 extrude from the slip zone (we did not use a PTFE containing ring for these tests). Once the sliding surface
189 was prepared, the normal stress was increased to 1.5 MPa and the samples were sheared for 0.26 mm during
190 each sliding event in the SHS experiment at a velocity of $2.6 \mu\text{m/s}$; the length of the hold time between the
191 sliding events was varied to determine the healing rate.

192

193 **2.2. Raman spectroscopy**

194 After the experiments the PTFE ring was removed and the sample holders were gently opened to
195 expose the sheared gouge sample. The surface of the gouge was then analyzed using Raman spectroscopy.
196 (Note that Raman spectra were acquired on the exposed gouge surface before it was impregnated with
197 epoxy resin and prepared for microstructural imaging). Raman spectra of the test samples were obtained
198 with a 514.5 nm Ar laser (Showa Optronics Co., Ltd.) and T64000 Raman system (Jobin Yvon Horiba).
199 The laser passed through a 40× objective and the laser power at the sample surface was set at 2–5 mW. The
200 scattered light was collected by backscattered geometry with a 25 μm pinhole and a holographic notch filter,
201 and finally dispersed using a 1800 grids/mm grating and analyzed by a Peltier cooled CCD detector
202 (SPECTRUM ONE, Jobin Yvon Horiba). Spatial resolution is about 1 μm, and wavenumber resolution is
203 about 1 cm⁻¹. Frequencies of the Raman bands were calibrated by measuring silicon standards.

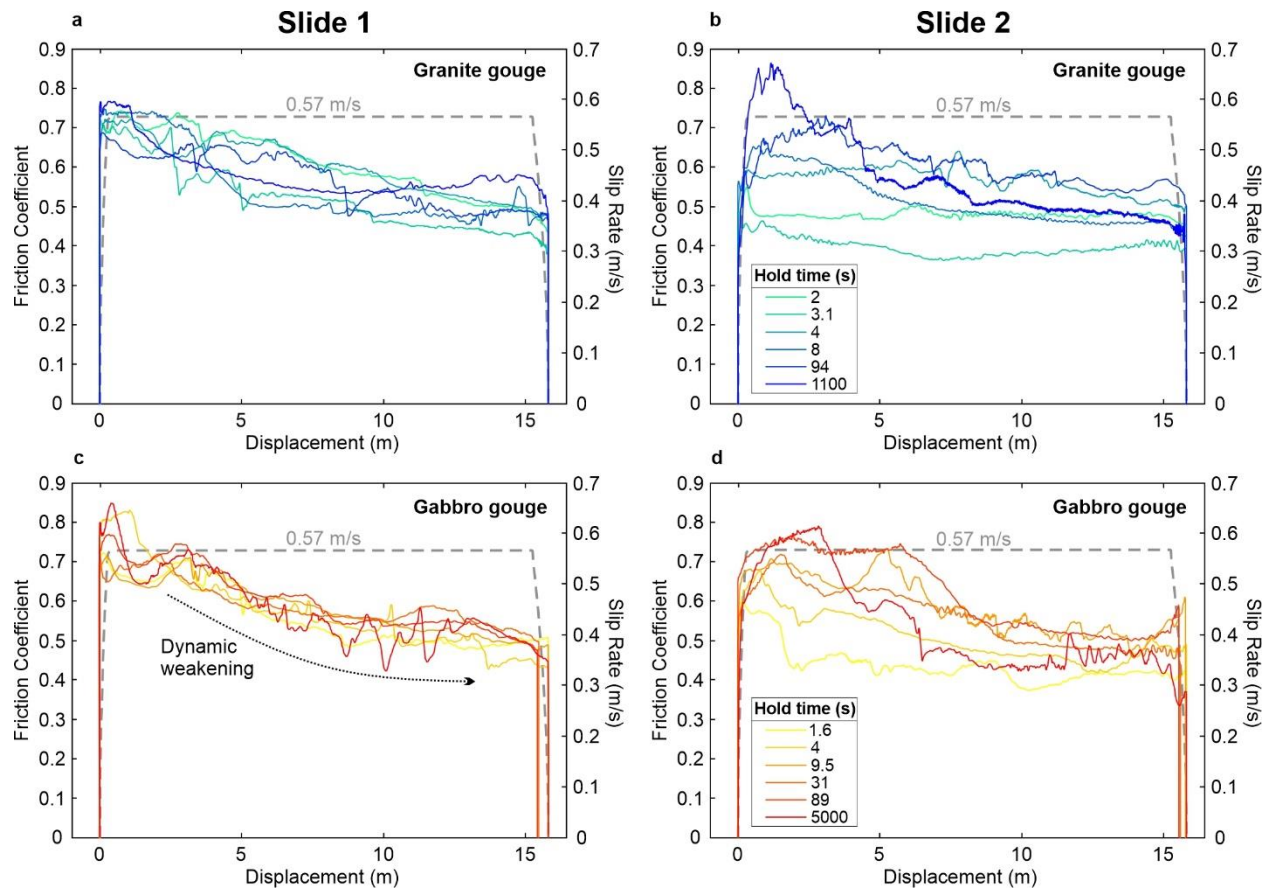
204

205 **3. Results**

206 **3.1. Friction data**

207 The frictional strength evolution of the granite and gabbro gouge samples is shown in Figure 3 for
208 both sliding events in the SHS experiments. During the first high-velocity sliding event (slide 1) the gouge
209 layers experience dynamic weakening with the friction coefficient (μ) decreasing by ~0.25, from a peak
210 value between 0.7-0.8, to a final value of ~0.5 after 15 m of slip (Fig. 3a and c). This amount of weakening
211 is comparable to previous experimental studies performed under similar normal stress and velocity
212 conditions (e.g., Seyler et al., 2020), with greater weakening (to $\mu \approx 0.2$) typically observed when gouges
213 are sheared under higher normal stresses (Pozzi et al., 2021; Seyler et al., 2020) or at faster sliding velocities
214 (Boulton et al., 2017; Yao et al., 2013) than in our experiments. During the static hold period between
215 sliding events in our experiments the gouge undergoes healing, with the peak friction of the second sliding

216 event (slide 2) being dependent on the duration of the hold period (Fig. 3b and d) – i.e., longer hold periods
 217 lead to higher peak friction values. During slide 2, after reaching their respective peak friction values, the
 218 gouge layers again experience dynamic weakening, returning to a final μ of ~ 0.5 after another 15 m of
 219 high-velocity slip.

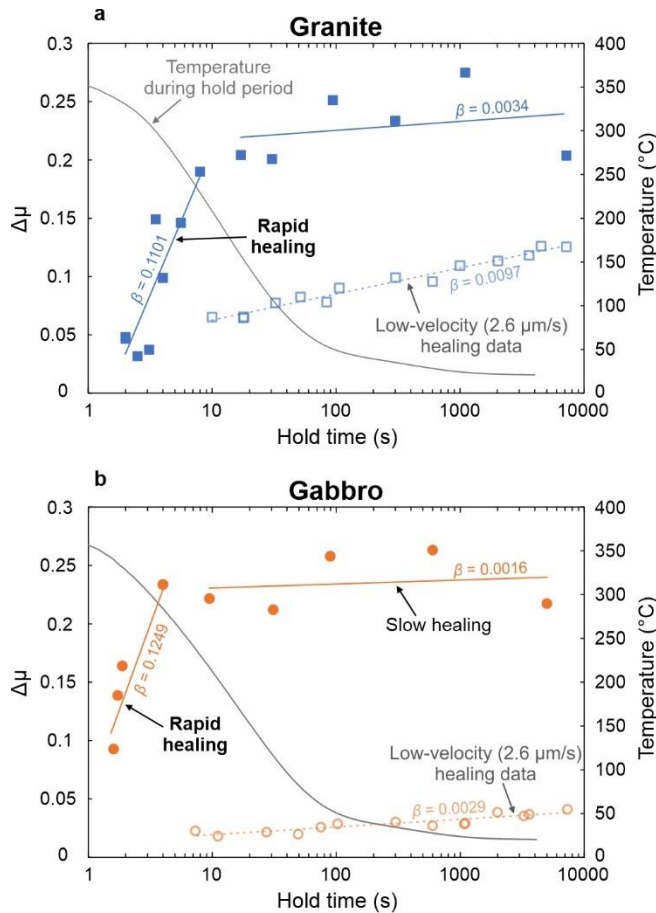


220
 221 **Figure 3:** Example mechanical data from the two high-velocity sliding events in the slide-hold-slide
 222 experiments. The plots show the evolution of the friction coefficient with displacement for the granite gouge
 223 during (a) the first sliding event (slide 1), and (b) the second sliding event (slide 2). The same data are
 224 shown for the gabbro gouge in panels (c) and (d), respectively. The velocity-displacement history during
 225 the experiments is shown by the grey dashed line. The gouge layers all show similar dynamic weakening
 226 during slide 1, with the friction coefficient decreasing by ~ 0.25 after 15 m of displacement. The peak friction
 227 during slide 2 is controlled by the duration of the static hold time between the sliding events, with longer
 228 hold times leading to higher peak friction.

229

230 The gouge samples recover their strength rapidly during the static hold period, as shown in Figure
231 4 where $\Delta\mu$ (the difference between the peak friction of slide 2 (μ_{p2}) and the final friction of slide 1 (μ_{f1}),
232 $\Delta\mu = \mu_{p2} - \mu_{f1}$; see also Fig. S1) is plotted against hold time. After around 20 s of static hold, the granite
233 gouge had recovered the majority of the strength it lost during slide 1, with the gabbro gouge healing even
234 more rapidly (<10 s of static hold). For comparison, healing data from low-velocity SHS experiments
235 performed on intact samples of granite and gabbro at slip rates of 2.6 $\mu\text{m/s}$ has been included in Figure 4
236 (see Methods for more details). The healing rate ($\beta = \Delta\mu/\Delta\log(t_h)$, where t_h is the hold time) is around
237 two orders of magnitude greater for the experiments performed at seismic slip velocities than those
238 performed at micrometer per second slip velocities (Fig. 4). After the initial rapid strength recovery in the
239 high-velocity tests ($\beta > 0.1$), the healing rate decreased to a rate that is comparable to those observed in the
240 low-velocity SHS experiments ($\beta < 0.01$), which is largely consistent with healing rates reported in
241 previous low-velocity friction studies on granitic and basaltic fault materials (Beeler et al., 1994; Carpenter
242 et al., 2016; Giacomel et al., 2021; Mitchell et al., 2013).

243 A major difference between high-velocity and low-velocity SHS experiments is that during high-
244 velocity slip there is a large temperature increase caused by shear heating, which is much less significant
245 during sliding at low-velocity. In order to measure the temperature evolution in our high-velocity SHS
246 experiments, we placed thermocouples next to the upper surface of the gouge layer on the stationary side
247 of the fault in some experiments (see Methods). We recorded peak temperatures of around 350-400 °C
248 during the high-velocity sliding events, with the temperature decaying as the samples cooled during the
249 hold period, returning to the ambient temperature in the laboratory after several minutes of static hold (Fig.
250 4). However, we find that the rapid frictional healing, which begins immediately after the initiation of the
251 hold period, occurred when the gouge layer was still relatively hot, at temperatures >200 °C (Fig. 4).



252

253 **Figure 4:** Frictional healing data from the high-velocity SHS experiments. The slide-hold-slide parameter
 254 $\Delta\mu$ is plotted against hold time for (a) granite gouge and (b) gabbro gouge. The gouges experience rapid
 255 healing immediately after the initiation of the hold period; the healing rate then decreases to a rate
 256 comparable to those observed in low-velocity SHS experiments. Healing data from experiments performed
 257 at 2.6 $\mu\text{m/s}$ has been included (hollow symbols) for comparison. The temperature evolution was monitored
 258 during the hold period (grey line); rapid healing occurs while the gouges are still relatively hot ($>200\text{ }^\circ\text{C}$)
 259 after the high-velocity first sliding event.

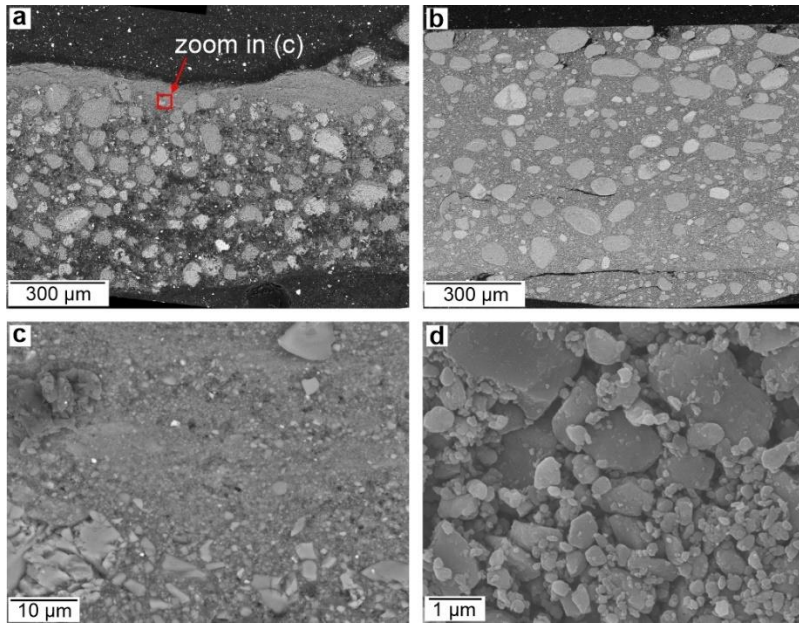
260

261 **3.2. Microstructural analysis and Raman spectroscopy**

262 We analyzed the microstructures of the sheared gouges by collecting backscatter electron (BSE)
 263 and secondary electron (SE) images using a JEOL JSM-6500F field emission scanning electron microscope

264 (FE-SEM). Fig. 5a-b shows BSE images of granite and gabbro gouge samples after the SHS experiments,
265 where the sheared layers have been cut perpendicular to the shear plane and parallel to the shearing direction
266 at a distance equal to $2/3$ of the sample radius. (Note that the gouge layers were vacuum impregnated with
267 a low-viscosity epoxy resin before being cut and polished ready for BSE imaging). The sheared gouges
268 display a texture of well-rounded larger relict grains surrounded by fine-grained highly comminuted
269 material, indicating that they have undergone a significant grain size reduction and particle rounding
270 when compared to the starting gouge material (see Fig. S2), with this likely occurring via mechanical
271 grinding (Sammis & Ben-Zion, 2008). In the granite gouge the deformation appears to be homogeneously
272 distributed across the layer (Fig. 5b), whereas the gabbro gouge displays evidence of a highly comminuted
273 localized zone at the boundary of the layer (Fig. 5a and c). Despite the apparent difference in localization
274 behavior between the different materials, their mechanical behavior is remarkably similar (Fig. 3),
275 suggesting that shear localization does not have a strong control on frictional strength evolution under these
276 experimental conditions. Our experiments were run under relatively low normal stress, previous studies
277 suggest that localization would become more prominent if the gouge layers were sheared under higher
278 normal stress (Bedford & Faulkner, 2021; Rempe et al., 2020), or if they were taken to greater shear strains
279 (Kaneki et al., 2020).

280



281

282 **Figure 5:** Backscatter electron images of (a) gabbro and (b) granite gouge layers recovered at the end of
 283 the SHS experiments. (c) Zoom of the localized zone within the gabbro gouge layer (from the red box in
 284 (a)). (d) Secondary electron image of the surface of the gabbro gouge layer showing the presence of sub-
 285 micron particles.

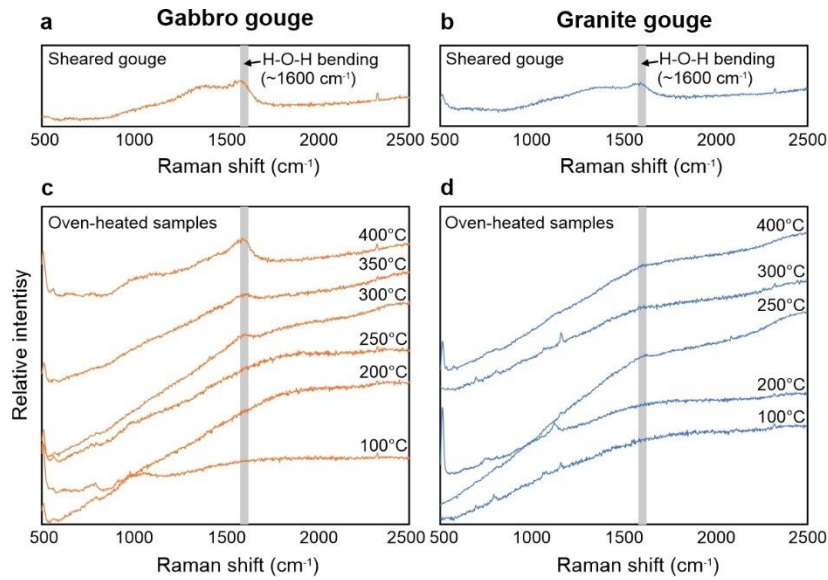
286

287 The rapid healing observed after sliding at seismic slip rates in our experiments (Fig. 4) must be
 288 caused by a strengthening of the frictional contacts in the gouge layer, possibly as a result of enhanced
 289 interfacial chemical bonding. To investigate further the possible causes of the rapid restrengthening, we
 290 analyzed the sheared gouges using Raman spectroscopy, as this provides information about the chemical
 291 structure of the gouge surface. We found that the gouges sheared at high-velocity all showed the appearance
 292 of a small broad peak in the Raman spectra at a wavenumber of $\sim 1600 \text{ cm}^{-1}$ (Fig. 6a and b), which
 293 corresponds to the bending vibrational mode of water (Kronenberg, 1994) adsorbed on the surface of the
 294 gouge. The bending mode is one of the three characteristic molecular vibration modes of water (along with
 295 the symmetric and asymmetric stretching modes), where the atomic bond angles are compressed and
 296 expanded in an oscillatory manner. The Raman peak associated with the bending vibrational mode was not

297 observed for the starting material or for samples sheared at low sliding velocities, only for samples that had
298 been subjected to sliding at seismic slip rates.

299 We hypothesize that the switch in vibration mode of adsorbed water is caused by a change in
300 chemical bonding on the gouge surface, potentially induced by elevated temperatures during high-velocity
301 shearing, which could be responsible for the rapid healing observed in the SHS experiments (Fig. 4). To
302 investigate this further, we heated undeformed samples of granite and gabbro in an oven to different
303 temperatures (leaving them for ~20 minutes at the target temperature), the samples were then removed from
304 the oven and left to cool at room atmosphere conditions (i.e., the same cooling conditions that the gouge
305 layers experienced during the hold period of the SHS experiments). We analyzed the oven-heated samples
306 using Raman spectroscopy and found the appearance of a small broad peak at $\sim 1600\text{ cm}^{-1}$ for samples that
307 had been heated to temperatures $\geq 250\text{ }^{\circ}\text{C}$ (Fig. 6c and d), which is similar to the temperatures that the gouge
308 layers experienced during high-velocity shearing where a similar Raman peak was observed (Fig. 6a and
309 b) and also the temperature conditions where rapid healing occurred (Fig. 4). We note that the size of the
310 adsorbed water peak in the oven-heated samples is often less than observed for the sheared gouge samples
311 (particularly for granite), which may be a result the sheared gouges having a much greater surface area due
312 to the presence of nanoparticles (Fig. 5d), producing a stronger Raman signal.

313



314

315 **Figure 6:** Raman spectra of the surface of the sheared gabbro (a) and granite (b) layers at the end of the
 316 SHS experiments. Both show a broad peak at a wavenumber of $\sim 1600\text{ cm}^{-1}$, indicating the bending
 317 vibrational mode of H-O-H. Panels (c) and (d) show Raman spectra for undeformed gabbro and granite
 318 samples heated to different temperatures in an oven and then left to cool under atmospheric humidity
 319 conditions. The broad peak at 1600 cm^{-1} only appears in samples that have been heated to temperatures
 320 $\geq 250\text{ }^{\circ}\text{C}$.

321

322 4. Discussion

323 4.1. Rapid fault healing

324 The frictional strength data from our high-velocity SHS experiments show that the fault gouges heal
 325 rapidly during static hold periods after shearing at seismic slip rates (Fig. 4), in comparison to typical
 326 healing rates observed in low-velocity SHS experiments performed at micrometer-per-second slip rates
 327 (Carpenter et al., 2016; Dieterich, 1972; Marone, 1997; Marone & Saffer, 2015). The rapid healing rates
 328 we observe for the granite and gabbro gouges in our study are a similar order to those observed in previous
 329 high-velocity SHS experiments on clay-carbonate-bearing gouges from the Longmenshan fault system
 330 (sheared at 0.8 MPa normal stress and a slip rate of 1.4 m/s (Yao et al., 2013)), suggesting that rapid healing

331 after high-velocity slip may be a universal phenomenon that is largely insensitive to the lithology of the
332 fault materials. Rapid healing ($\beta > 0.1$) has also been observed during previous SHS experiments performed
333 at subseismic slip rates (85 mm/s) on bare surfaces (i.e., no gouge, rock-to-rock experiments) of gabbro and
334 granite (Mizoguchi et al., 2006, 2009). We also performed some high-velocity (0.57 m/s) bare-surface SHS
335 experiments using intact samples of granite and gabbro to see whether the healing rates reported by
336 Mizoguchi et al., (2009) would increase at higher slip velocities. However, whereas Mizoguchi et al., (2009)
337 found rapid healing during the static hold periods in their SHS experiments at subseismic slip velocities,
338 we found that during our high-velocity SHS experiments the rock-to-rock samples recovered almost all of
339 their strength during the deceleration phase while the fault was still slipping (Fig. S3), meaning that the
340 healing rate during the static hold period could not be analyzed. Frictional restrengthening during
341 deceleration (similar to coseismic restrengthening in Fig. 1) is commonly observed in high-velocity
342 experiments performed on bare surfaces (Harbord et al., 2021; Proctor et al., 2014; Violay et al., 2019), and
343 implies that the healing mechanisms in operation are able to act so efficiently that the strength recovery
344 occurs while the sample is still being sheared. The efficient strength recovery in high-velocity bare surface
345 experiments may be due to the highly localized nature of these faults, whereas the deformation in gouge
346 experiments is typically distributed across a broader zone (e.g., Fig. 5) which may lead to less efficient
347 strength recovery, resulting in the majority of the healing to occur during the static hold period once slip
348 has ceased (Fig. 4). However, it should be noted that partial strength recovery during deceleration is
349 sometimes also observed in high-velocity experiments performed on gouge samples, particularly if the
350 deformation is highly localized within the gouge layer (e.g., Sone & Shimamoto, 2009).

351 Dynamic weakening during the high-velocity shearing events in our experiments (Fig. 3) is likely
352 caused by a combination of flash heating at asperity contacts (Passelègue et al., 2016; Rice, 2006) and the
353 formation of amorphous wear materials in the gouge (Rowe et al., 2019). X-ray diffraction analysis of the
354 sheared gouges confirms the presence of amorphous material that was not present in the starting materials
355 (Fig. S4). The microstructures of the sheared gouges (Fig. 5) show no evidence of other weakening

356 mechanisms that have been reported in previous studies such as frictional melting (Hirose & Shimamoto,
357 2005), silica-gel formation (Goldsby & Tullis, 2002) or grain-size sensitive flow (De Paola et al., 2015;
358 Pozzi et al., 2021). Fault restrengthening during the hold periods is likely caused by the reformation of
359 bonds at asperity contacts in the gouge material. There are two prevailing hypotheses for the time-dependent
360 strengthening of frictional contacts during fault healing: (i) an increase in real contact area by asperity creep
361 (Dieterich & Kilgore, 1994), often referred to as the contact ‘quantity’ hypothesis, or (ii) the formation of
362 chemical bonds across the asperity interface (Li et al., 2011; Thom et al., 2018), often referred to as the
363 contact ‘quality’ hypothesis.

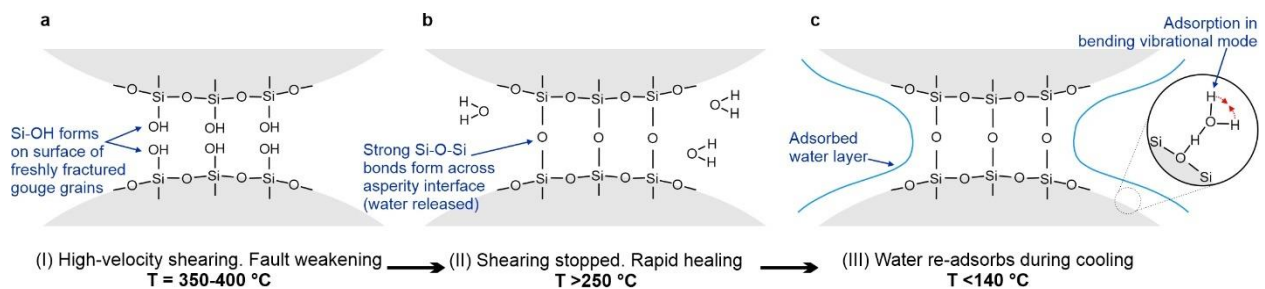
364 If we first consider asperity creep, it is plausible that this process would be more active after seismic
365 slip, as creep is temperature-sensitive and the rapid healing we observe occurs immediately after high-
366 velocity slip while the gouge is still relatively hot (>200 °C, Fig. 4). The likely mechanisms that could
367 facilitate asperity creep are either solution-transfer processes (Rutter, 1983) or indentation creep (Scholz &
368 Engelder, 1976). Solution-transfer is unlikely to be a dominant mechanism in our experiments as they were
369 run without a pore-fluid (i.e., room atmosphere conditions), therefore there is no solute to transfer chemical
370 species. Furthermore, previous fault healing experiments under hydrothermal conditions, where solution-
371 transfer processes are operative, show complex healing behavior (van den Ende & Niemeijer, 2019; Jeppson
372 & Lockner, 2022; Karner et al., 1997; Nakatani & Scholz, 2004) that is quite different to the healing trends
373 we observe in our data (Fig. 4). Indentation creep can operate under atmospheric conditions in the absence
374 of a pore-fluid (Frye & Marone, 2002), however, although previous low-velocity fault healing experiments
375 at elevated temperatures (up to 550°C) under room humidity conditions indicate some temperature-
376 dependence on healing rate (Mitchell et al., 2013; Nakatani, 2001), the effect is relatively minor (for intact
377 granite Mitchell et al., (2013) found that β increases from 0.016 at room temperature to 0.021 at 500°C)
378 and insufficient to explain the rapid healing in our experiments. It is therefore unlikely that an increase in
379 the real contact area via asperity creep is the cause of the rapid restrengthening we observe during the static
380 hold periods.

381 Alternatively, rapid healing may be caused by enhanced chemical bonding across contacting
382 asperity interfaces. Our Raman data reveal a change in chemical bonding on the surface of the gouges
383 sheared at high-velocity, with a switch in the vibrational mode of adsorbed water to the H-O-H bending
384 mode, which only occurs after sample has been heated to temperatures ≥ 250 °C (Fig. 6c-d). Although we
385 observe a change in adsorbed water properties, we do not expect the adsorbed water itself to be responsible
386 for the rapid healing, as rapid healing occurs at temperatures > 200 °C (Fig. 4) where water would be in the
387 vapor state and desorbed from the gouge surface (Reches & Lockner, 2010). Instead, we hypothesize that
388 the rapid healing is a result of hydrogen bonding on the surface of the sheared gouge materials, which
389 subsequently causes water to re-adsorb in the bending vibrational mode once the gouge has cooled to
390 sufficiently low temperatures (< 140 °C) (Reches & Lockner, 2010) during the hold period. Hydrogen
391 bonding can arise between hydroxylated silanol (Si-OH) surfaces (Michalske & Fuller, 1985), which are
392 readily formed on freshly cleaved surfaces of silicate materials during frictional slip (Hirose et al., 2011;
393 Kronenberg, 1994; Rowe et al., 2019) (Fig. 7a). Once slip has stopped, the formation of hydrogen bonds
394 between silanol surfaces can take place on very short timescales ($< 10^{-2}$ s) (Liu & Szlufarska, 2012).
395 Therefore, if hydrogen bonding occurs during the first few seconds of static hold in our experiments, it
396 could be responsible for the rapid increase in friction we observe. Furthermore, at elevated temperatures,
397 like those produced by shear heating in our experiments, silanol groups on opposite sides of an asperity
398 interface can react to form strong covalent siloxane (Si-O-Si) bonds (Shioji et al., 2001; Vigil et al., 1994)
399 (Fig. 7b). Previous molecular dynamics simulations of silica-silica interfaces have shown that siloxane bond
400 formation provides a plausible explanation for frictional healing, with frictional strength being
401 approximately proportional to the number of siloxane bonds (Li et al., 2014) and the kinetics of interfacial
402 bond formation leading to a logarithmic time-dependent increase in strength (Liu & Szlufarska, 2012), as
403 observed in SHS experiments (Fig. 4). Therefore, we postulate that rapid healing after high-velocity slip is
404 caused by either hydrogen or siloxane bond formation (or a combination of both) at asperity contacts in the
405 sheared gouges. Once the gouge has cooled to sufficiently low temperature water will re-adsorb (Reches &
406 Lockner, 2010) (Fig. 7c). The vibrational motions of water molecules are sensitive to local hydrogen

407 bonding on the adsorbent surface (Kronenberg, 1994; Shioji et al., 2001), thus the switch to the H-O-H
 408 bending mode we observe on the sheared gouges likely results from changes in the hydrogen bonding on
 409 the gouge surface that occur during/after high-velocity slip while the gouge is still hot, hence why the
 410 change in adsorbed water properties is only observed in samples that have been heated to temperatures
 411 $>250\text{ }^{\circ}\text{C}$ (Fig. 6c-d) and not in the samples sheared at low velocity where the temperature increase was low.

412 The hypothesis that rapid healing is caused by enhanced hydrogen bonding is also supported by the
 413 experimental results of Mizoguchi et al., (2006), who find that rapid healing is suppressed in their bare
 414 surface SHS experiments on intact gabbro samples (sheared at 85 mm/s) when they are performed in a
 415 nitrogen atmosphere, instead of at room humidity conditions. Although Mizoguchi et al., (2006, 2009)
 416 interpret this to mean that rapid healing is caused by water adsorption onto the fault surface during the static
 417 hold period (they calculate a maximum temperature due to shear heating of $\sim 100\text{ }^{\circ}\text{C}$ in their subseismic
 418 SHS experiments), we have shown that water adsorption cannot be responsible, as the rapid healing in our
 419 high-velocity experiments occurs early during the static hold period (Fig. 4) while the sample temperature
 420 is too high for water adsorption ($>200\text{ }^{\circ}\text{C}$). Instead, we postulate that the suppressed healing in the nitrogen
 421 experiments of Mizoguchi et al., (2006) is due to a lack of hydrogen bonding in this environment. When
 422 there is no moisture available, hydroxylated silanol (SiOH) will be unable to form on the surface of the
 423 fault materials during shearing, which will in turn limit any hydrogen bonding across asperity interfaces
 424 during the static hold period. The results of Mizoguchi et al., (2006, 2009) are therefore consistent with our
 425 hypothesis that rapid healing is caused by enhanced chemical bond formation across asperity interfaces.

426



428 **Figure 7:** Schematic cartoon showing the evolution of chemical bonding during and after high-velocity
429 slip. (a) Silanol bonds (Si-OH) form on freshly fractured gouge surfaces during high-velocity slip. During
430 the hold period, once fault slip has ceased, we hypothesize that rapid healing occurs as a result of either
431 hydrogen bonding between adjacent silanol surfaces, or (b) the formation of strong siloxane bonds across
432 the asperity interface. (c) Once the gouge has cooled to temperatures <140 °C during the hold period,
433 water re-adsorbs onto the surface in the bending vibrational mode.

434

435 **4.2. Implications for fault strength evolution and earthquake recurrence**

436 Regardless of the underlying restrengthening mechanism, our data clearly show that fault materials
437 heal rapidly after seismic slip, which has important implications for our understanding of the earthquake
438 cycle. Rapid healing may explain why geophysical observations suggest some faults regain their strength
439 early during interseismic periods after large earthquakes (Magen et al., 2020; Tadokoro & Ando, 2002; Xue
440 et al., 2013). Fast-acting healing mechanisms, like those in operation during our experiments, potentially
441 also operate during coseismic slip on natural faults, particularly when slip occurs heterogeneously along
442 the fault such as during the propagation of pulse-like ruptures (Heaton, 1990; Lambert et al., 2021; Wang
443 & Barbot, 2023). The passage of a rupture pulse requires rapid healing in the just-slipped portions of the
444 fault (Perrin et al., 1995), in order for them to stay locked and prevent further slip as they are reloaded by
445 waves from the actively slipping regions elsewhere along the fault. It is plausible that the rapid healing
446 mechanisms in our experiments become faster acting at the pressure-temperature conditions associated with
447 seismogenic depths in nature, meaning that they could potentially contribute to the generation of pulse-like
448 ruptures. Future studies at higher normal stress and ambient temperatures, as well as in the presence of pore
449 fluids, are required to investigate how the rates of frictional healing evolve with depth in the Earth's crust.
450 Results from recent dynamic rupture experiments further highlight the complex interplay between rapid
451 weakening and healing processes that occur in gouge samples during dynamic rupture propagation (Rubino
452 et al., 2022).

453 Rapid fault strength recovery immediately following a seismic event suggests that earthquake
454 recurrence is not necessarily controlled by continuous restrengthening over time during interseismic
455 periods. Instead, if the majority of strength is recovered early during the interseismic period, as implied by
456 our results, then earthquake recurrence on natural faults may be more strongly controlled by far-field
457 tectonic loading (i.e., when the buildup of stress applied to the fault exceeds the strength an earthquake may
458 occur). Alternatively, other time-dependent processes in operation during interseismic periods may
459 influence earthquake recurrence. For example, over typical recurrence intervals of hundreds of years, fault
460 cohesion will also increase by longer timescale processes such as cementation and pressure solution (van
461 den Ende & Niemeijer, 2019; Muhuri et al., 2003; Tenthorey & Cox, 2006). The resulting increase in
462 cohesion and lithification of the fault gouge will not only contribute to the fault strength evolution, but will
463 also influence the frictional stability of the gouge materials, with more cohesive materials often displaying
464 rate-weakening behavior required for earthquake nucleation (Ikari & Hüpers, 2021; Roesner et al., 2020).
465 It is plausible that transitions from rate-strengthening to rate-weakening behavior may occur as the gouge
466 materials become more lithified during interseismic periods, potentially leading to earthquake recurrence
467 once the frictional properties have evolved to a state that promotes earthquake nucleation and unstable slip.

468

469 **5. Conclusions**

470 In summary, we find that faults regain their strength rapidly after experiencing dynamic weakening
471 during seismic slip. After the initial rapid increase in strength, the healing rate decreases to a rate that is
472 comparable to those observed in low-velocity friction experiments. Rapid healing occurs while the gouge
473 is still relatively hot from shear heating, and is likely promoted by enhanced chemical bonding across
474 contacting asperity interfaces. Further experimental and theoretical studies are needed to investigate the
475 kinetics of interfacial reactions over the range of stress, temperature and pore fluid conditions that faults
476 experience during and after earthquake slip, to understand better strength recovery at seismogenic depths.
477 Our findings motivate further study aimed at the quantification of rapid healing mechanisms and

478 incorporation into larger-scale constitutive laws for modelling dynamic fault processes, to provide insight
479 into the driving mechanisms of earthquake rupture and arrest, and hence seismic hazard.

480

481 **Acknowledgments**

482 We are grateful to T. Suzuki and O. Tadai for technical support with the experiments and analyses. This
483 work was supported by a Japan Society for the Promotion of Science (JSPS) International Research
484 Fellowship and JSPS KAKENHI Grant Numbers JP20F20786 and JP19K21907. The associated
485 experimental data files for this research can be accessed at:
486 <https://data.mendeley.com/datasets/rw3ndtwkgt/1>

487

488 **References**

- 489 Bedford, J. D., & Faulkner, D. R. (2021). The role of grain size and effective normal stress on localization
490 and the frictional stability of simulated quartz gouge. *Geophysical Research Letters*, *48*(7),
491 e2020GL092023. <https://doi.org/10.1029/2020gl092023>
- 492 Beeler, N. M., Tullis, T. E., & Weeks, J. D. (1994). The roles of time and displacement in the evolution
493 effect in rock friction. *Geophysical Research Letters*, *21*(18), 1987–1990.
494 <https://doi.org/10.1029/94GL01599>
- 495 Boulton, C., Yao, L., Faulkner, D. R., Townend, J., Toy, V. G., Sutherland, R., et al. (2017). High-
496 velocity frictional properties of Alpine Fault rocks: Mechanical data, microstructural analysis, and
497 implications for rupture propagation. *Journal of Structural Geology*, *97*, 71–92.
498 <https://doi.org/10.1016/j.jsg.2017.02.003>
- 499 Carpenter, B. M., Ikari, M. J., & Marone, C. (2016). Laboratory observations of time-dependent frictional
500 strengthening and stress relaxation in natural and synthetic fault gouges. *Journal of Geophysical*

501 *Research: Solid Earth*, 121, 1183–1201. <https://doi.org/10.1002/2015JB012136>

502 De Paola, N., Holdsworth, R. E., Viti, C., Collettini, C., & Bullock, R. (2015). Can grain size sensitive
503 flow lubricate faults during the initial stages of earthquake propagation? *Earth and Planetary Science*
504 *Letters*, 431, 48–58. <https://doi.org/10.1016/j.epsl.2015.09.002>

505 Dieterich, J. H. (1972). Time-dependent friction in rocks. *Journal of Geophysical Research*, 77(20),
506 3690–3697. <https://doi.org/10.1029/JB077i020p03690>

507 Dieterich, J. H., & Kilgore, B. D. (1994). Direct observation of frictional contacts: New insights for state-
508 dependent properties. *Pure and Applied Geophysics*, 143, 283–302.
509 <https://doi.org/10.1007/BF00874332>

510 Di Toro, G., Han, R., Hirose, T., De Paola, N., Nielsen, S., Mizoguchi, K., et al. (2011). Fault lubrication
511 during earthquakes. *Nature*, 471, 494–498. <https://doi.org/10.1038/nature09838>

512 Frye, K. M., & Marone, C. (2002). Effect of humidity on granular friction at room temperature. *Journal*
513 *of Geophysical Research*, 107(B11), 2309. <https://doi.org/10.1029/2001jb000654>

514 Giacomel, P., Ruggieri, R., Scuderi, M. M., Spagnuolo, E., Di Toro, G., & Collettini, C. (2021). Frictional
515 properties of basalt experimental faults and implications for volcano-tectonic settings and geo-
516 energy sites. *Tectonophysics*, 811, 228883. <https://doi.org/10.1016/j.tecto.2021.228883>

517 Goldsby, D. L., & Tullis, T. E. (2002). Low frictional strength of quartz rocks at subseismic slip rates.
518 *Geophysical Research Letters*, 29(17), 1844. <https://doi.org/10.1029/2002GL015240>

519 Han, R., Shimamoto, T., Hirose, T., Ree, J. H., & Ando, J. (2007). Ultralow friction of carbonate faults
520 caused by thermal decomposition. *Science*, 316(5826), 878–881.
521 <https://doi.org/10.1126/science.1139763>

522 Harbord, C., Brantut, N., Spagnuolo, E., & Di Toro, G. (2021). Fault friction during simulated seismic
523 slip pulses. *Journal of Geophysical Research: Solid Earth*, 126, e2021JB022149.

524 <https://doi.org/10.1029/2021JB022149>

525 Heaton, T. H. (1990). Evidence for and implications of self-healing pulses of slip in earthquake rupture.
526 *Physics of the Earth and Planetary Interiors*, 64, 1–20. <https://doi.org/10.1016/0031->
527 9201(90)90002-F

528 Hirose, T., & Shimamoto, T. (2005). Growth of molten zone as a mechanism of slip weakening of
529 simulated faults in gabbro during frictional melting. *Journal of Geophysical Research*, 110, B05202.
530 <https://doi.org/10.1029/2004JB003207>

531 Hirose, T., Kawagucci, S., & Suzuki, K. (2011). Mechanoradical H₂ generation during simulated faulting:
532 Implications for an earthquake-driven subsurface biosphere. *Geophysical Research Letters*, 38,
533 L17303. <https://doi.org/10.1029/2011GL048850>

534 Hunfeld, L. B., Chen, J., Niemeijer, A. R., Ma, S., & Spiers, C. J. (2021). Seismic slip-pulse experiments
535 simulate induced earthquake rupture in the Groningen gas field. *Geophysical Research Letters*, 48,
536 e2021GL092417. <https://doi.org/10.1029/2021GL092417>

537 Ikari, M. J., & Hüpers, A. (2021). Velocity-weakening friction induced by laboratory-controlled
538 lithification. *Earth and Planetary Science Letters*, 554, 116682.
539 <https://doi.org/10.1016/j.epsl.2020.116682>

540 Jeppson, T., & Lockner, D. (2022). Impact of fluid-rock interaction on strength and hydraulic
541 transmissivity evolution in shear fractures under hydrothermal conditions. In *47th Workshop on*
542 *Geothermal Reservoir Engineering*. Stanford, California.

543 Kanamori, H., & Allen, C. R. (1986). Earthquake repeat time and average stress drop. In S. Das, J.
544 Boatwright, & C. H. Scholz (Eds.), *Earthquake Source Mechanics* (Vol. 37, pp. 227–235).
545 Washington D.C.: American Geophysical Union. <https://doi.org/10.1029/GM037p0227>

546 Kaneki, S., Oohashi, K., Hirono, T., & Noda, H. (2020). Mechanical amorphization of synthetic fault
547 gouges during rotary-shear friction experiments at subseismic to seismic slip velocities. *Journal of*

548 *Geophysical Research: Solid Earth*, 125, e2020JB019956. <https://doi.org/10.1029/2020JB019956>

549 Karner, S. L., Marone, C., & Evans, B. (1997). Laboratory study of fault healing and lithification in
550 simulated fault gouge under hydrothermal conditions. *Tectonophysics*, 277, 41–55.
551 [https://doi.org/10.1016/S0040-1951\(97\)00077-2](https://doi.org/10.1016/S0040-1951(97)00077-2)

552 Kronenberg, A. K. (1994). Hydrogen speciation and chemical weakening of quartz. In P. J. Heaney, C. T.
553 Prewitt, & G. V Gibbs (Eds.), *Silica: Physical Behaviour, Geochemistry and Materials Applications*
554 (pp. 123–176). Mineralogical Society of America.

555 Lambert, V., Lapusta, N., & Perry, S. (2021). Propagation of large earthquakes as self-healing pulses or
556 mild cracks. *Nature*, 591, 252–258. <https://doi.org/10.1038/s41586-021-03248-1>

557 Li, A., Liu, Y., & Szlufarska, I. (2014). Effects of interfacial bonding on friction and wear at silica/silica
558 interfaces. *Tribology Letters*, 56, 481–490. <https://doi.org/10.1007/s11249-014-0425-x>

559 Li, Q., Tullis, T. E., Goldsby, D., & Carpick, R. W. (2011). Frictional ageing from interfacial bonding and
560 the origins of rate and state friction. *Nature*, 480, 233–236. <https://doi.org/10.1038/nature10589>

561 Li, Y.-G., Chen, P., Cochran, E. S., Vidale, J. E., & Burdette, T. (2006). Seismic evidence for rock
562 damage and healing on the San Andreas Fault associated with the 2004 M 6.0 Parkfield earthquake.
563 *Bulletin of the Seismological Society of America*, 96(4B), S349–S363.
564 <https://doi.org/10.1785/0120050803>

565 Liu, Y., & Szlufarska, I. (2012). Chemical origins of frictional aging. *Physical Review Letters*,
566 109(186102). <https://doi.org/10.1103/PhysRevLett.109.186102>

567 Magen, Y., Ziv, A., Inbal, A., Baer, G., & Hollingsworth, J. (2020). Fault rerupture during the July 2019
568 Ridgecrest earthquake pair from joint slip inversion of InSAR, optical imagery, and GPS. *Bulletin of*
569 *the Seismological Society of America*, 110, 1627–1643. <https://doi.org/10.1785/0120200024>

570 Marone, C. (1997). On the rate of frictional healing and the constitutive law for time- and slip-dependent

571 friction. *International Journal of Rock Mechanics & Mining Sciences*, 34(3–4), 187.e1-187.e17.
572 [https://doi.org/10.1016/S1365-1609\(97\)00054-3](https://doi.org/10.1016/S1365-1609(97)00054-3)

573 Marone, C., & Saffer, D. M. (2015). The mechanics of frictional healing and slip instability during the
574 seismic cycle. In G. Schubert (Ed.), *Treatise on Geophysics* (2nd ed., Vol. 4, pp. 111–138). Elsevier.
575 <https://doi.org/10.1016/B978-0-444-53802-4.00092-0>

576 Marone, C., Vidale, J. E., & Ellsworth, W. L. (1995). Fault healing inferred from time dependent
577 variations in source properties of repeating earthquakes. *Geophysical Research Letters*, 22(22),
578 3095–3098. <https://doi.org/10.1029/95GL03076>

579 McLaskey, G. C., Thomas, A. M., Glaser, S. D., & Nadeau, R. M. (2012). Fault healing promotes high-
580 frequency earthquakes in laboratory experiments and on natural faults. *Nature*, 491, 101–104.
581 <https://doi.org/10.1038/nature11512>

582 Michalske, T. A., & Fuller, E. R. (1985). Closure and repropagation of healed cracks in silicate glass.
583 *Journal of the American Ceramic Society*, 68(11), 586–590. [https://doi.org/10.1111/j.1151-](https://doi.org/10.1111/j.1151-2916.1985.tb16160.x)
584 [2916.1985.tb16160.x](https://doi.org/10.1111/j.1151-2916.1985.tb16160.x)

585 Mitchell, E. K., Fialko, Y., & Brown, K. M. (2013). Temperature dependence of frictional healing of
586 Westerly granite: Experimental observations and numerical simulations. *Geochemistry, Geophysics,*
587 *Geosystems*, 14(3), 567–582. <https://doi.org/10.1029/2012GC004241>

588 Mizoguchi, K., Hirose, T., Shimamoto, T., & Fukuyama, E. (2006). Moisture-related weakening and
589 strengthening of a fault activated at seismic slip rates. *Geophysical Research Letters*, 33, L16319.
590 <https://doi.org/10.1029/2006GL026980>

591 Mizoguchi, K., Hirose, T., Shimamoto, T., & Fukuyama, E. (2009). Fault heals rapidly after dynamic
592 weakening. *Bulletin of the Seismological Society of America*, 99(6), 3470–3474.
593 <https://doi.org/10.1785/0120080325>

594 Muhuri, S. K., Dewers, T. A., Scott Jr., T. E., & Reches, Z. (2003). Interseismic fault strengthening and

595 earthquake-slip instability: Friction or cohesion? *Geology*, 31(10), 881–884.
596 <https://doi.org/10.1130/G19601.1>

597 Nakatani, M. (2001). Conceptual and physical clarification of rate and state friction: Frictional sliding as a
598 thermally activated rheology. *Journal of Geophysical Research*, 106(B7), 13347–13380.
599 <https://doi.org/10.1029/2000JB900453>

600 Nakatani, M., & Scholz, C. H. (2004). Frictional healing of quartz gouge under hydrothermal conditions:
601 1. Experimental evidence for solution transfer healing mechanism. *Journal of Geophysical*
602 *Research*, 109, B07201. <https://doi.org/10.1029/2001JB001522>

603 Orellana, L. F., Scuderi, M. M., Collettini, C., & Violay, M. (2018). Do scaly clays control seismicity on
604 faulted shale rocks? *Earth and Planetary Science Letters*, 488, 59–67.
605 <https://doi.org/10.1016/j.epsl.2018.01.027>

606 Passelègue, F. X., Spagnuolo, E., Violay, M., Nielsen, S., Di Toro, G., & Schubnel, A. (2016). Frictional
607 evolution, acoustic emissions activity, and off-fault damage in simulated faults sheared at seismic
608 slip rates. *Journal of Geophysical Research: Solid Earth*, 121(10), 7490–7513.
609 <https://doi.org/10.1002/2016JB012988>

610 Pei, S., Niu, F., Ben-Zion, Y., Sun, Q., Liu, Y., Xue, X., et al. (2019). Seismic velocity reduction and
611 accelerated recovery due to earthquakes on the Longmenshan fault. *Nature Geoscience*, 12, 387–
612 392. <https://doi.org/10.1038/s41561-019-0347-1>

613 Perrin, G., Rice, J. R., & Zheng, G. (1995). Self-healing slip pulse on a frictional surface. *Journal of the*
614 *Mechanics and Physics of Solids*, 43(9), 1461–1495. [https://doi.org/10.1016/0022-5096\(95\)00036-I](https://doi.org/10.1016/0022-5096(95)00036-I)

615 Pozzi, G., De Paola, N., Nielsen, S. B., Holdsworth, R. E., Tesei, T., Thieme, M., & Demouchy, S.
616 (2021). Coseismic fault lubrication by viscous deformation. *Nature Geoscience*, 14, 437–442.
617 <https://doi.org/10.1038/s41561-021-00747-8>

618 Proctor, B. P., Mitchell, T. M., Hirth, G., Goldsby, D., Zorzi, F., Platt, J. D., & Di Toro, G. (2014).

619 Dynamic weakening of serpentinite gouges and bare surfaces at seismic slip rates. *Journal of*
620 *Geophysical Research: Solid Earth*, 119, 8107–8131. <https://doi.org/10.1002/2014JB011057>

621 Reches, Z., & Lockner, D. A. (2010). Fault weakening and earthquake instability by powder lubrication.
622 *Nature*, 467, 452–455. <https://doi.org/10.1038/nature09348>

623 Rempe, M., Di Toro, G., Mitchell, T. M., Smith, S. A. F., Hirose, T., & Renner, J. (2020). Influence of
624 effective stress and pore fluid pressure on fault strength and slip localization in carbonate slip zones.
625 *Journal of Geophysical Research: Solid Earth*, 125, e2020JB019805.
626 <https://doi.org/10.1029/2020JB019805>

627 Rice, J. R. (2006). Heating and weakening of faults during earthquake slip. *Journal of Geophysical*
628 *Research*, 111(B05311). <https://doi.org/10.1029/2005JB004006>

629 Roesner, A., Ikari, M. J., Saffer, D. M., Stanislawski, K., Eijsink, A. M., & Kopf, A. J. (2020). Friction
630 experiments under in-situ stress reveal unexpected velocity-weakening in Nankai accretionary prism
631 samples. *Earth and Planetary Science Letters*, 538(116180).
632 <https://doi.org/10.1016/j.epsl.2020.116180>

633 Rowe, C. D., Lamothe, K., Rempe, M., Andrews, M., Mitchell, T. M., Di Toro, G., et al. (2019).
634 Earthquake lubrication and healing explained by amorphous nanosilica. *Nature Communications*,
635 10(1), 1–11. <https://doi.org/10.1038/s41467-018-08238-y>

636 Rubino, V., Lapusta, N., & Rosakis, A. J. (2022). Intermittent lab earthquakes in dynamically weakening
637 fault gouge. *Nature*, 606, 922–929. <https://doi.org/10.1038/s41586-022-04749-3>

638 Rutter, E. H. (1983). Pressure solution in nature, theory and experiment. *Journal of the Geological*
639 *Society*, 140(5), 725–740. <https://doi.org/10.1144/gsjgs.140.5.0725>

640 Sammis, C. G., & Ben-Zion, Y. (2008). Mechanics of grain-size reduction in fault zones. *Journal of*
641 *Geophysical Research: Solid Earth*, 113(B02306). <https://doi.org/10.1029/2006JB004892>

642 Scholz, C. H., & Engelder, J. T. (1976). The role of asperity indentation and ploughing in rock friction - I.
643 Asperity creep and stick-slip. *International Journal of Rock Mechanics and Mining Sciences and*
644 *Geomechanical Abstracts*, 13(5), 149–154. [https://doi.org/10.1016/0148-9062\(76\)90819-6](https://doi.org/10.1016/0148-9062(76)90819-6)

645 Scholz, C. H., Aviles, C. A., & Wesnousky, S. G. (1986). Scaling differences between large interplate and
646 intraplate earthquakes. *Bulletin of the Seismological Society of America*, 76(1), 65–70.
647 <https://doi.org/10.1785/BSSA0760010065>

648 Seyler, C. E., Kirkpatrick, J. D., Savage, H. M., Hirose, T., & Faulkner, D. R. (2020). Rupture to the
649 trench? Frictional properties and fracture energy of incoming sediments at the Cascadia subduction
650 zone. *Earth and Planetary Science Letters*, 546, 116413. <https://doi.org/10.1016/j.epsl.2020.116413>

651 Shioji, S., Kawaguchi, M., Hayashi, Y., Tokami, K., & Yamamoto, H. (2001). Rehydroxylation of
652 dehydrated silica surfaces by water vapor adsorption. *Advanced Powder Technology*, 12(3), 331–
653 342. <https://doi.org/10.1163/156855201750537884>

654 Shreedharan, S., Saffer, D., Wallace, L. M., & Williams, C. (2023). Ultralow frictional healing explains
655 recurring slow slip events. *Science*, 379(6633), 712–717. <https://doi.org/10.1126/science.adf4930>

656 Sone, H., & Shimamoto, T. (2009). Frictional resistance of faults during accelerating and decelerating
657 earthquake slip. *Nature Geoscience*, 2, 705–708. <https://doi.org/10.1038/ngeo637>

658 Tadokoro, K., & Ando, M. (2002). Evidence for rapid fault healing derived from temporal changes in S
659 wave splitting. *Geophysical Research Letters*, 29(4), 1047. <https://doi.org/10.1029/2001GL013644>

660 Tanikawa, W., Mukoyoshi, H., & Tadai, O. (2012). Experimental investigation of the influence of slip
661 velocity and temperature on permeability during and after high-velocity fault slip. *Journal of*
662 *Structural Geology*, 38, 90–101. <https://doi.org/10.1016/j.jsg.2011.08.013>

663 Tenthorey, E., & Cox, S. F. (2006). Cohesive strengthening of fault zones during the interseismic period:
664 An experimental study. *Journal of Geophysical Research*, 111(B09202).
665 <https://doi.org/10.1029/2005JB004122>

666 Thom, C. A., Carpick, R. W., & Goldsby, D. L. (2018). Constraints on the physical mechanism of
667 frictional aging from nanoindentation. *Geophysical Research Letters*, *45*, 13306–13311.
668 <https://doi.org/10.1029/2018GL080561>

669 Tsutsumi, A., & Shimamoto, T. (1997). High-velocity frictional properties of gabbro. *Geophysical*
670 *Research Letters*, *24*(6), 699–702. <https://doi.org/10.1029/97GL00503>

671 Tullis, T. E. (2015). Mechanisms for friction of rock at earthquake slip rates. In G. Schubert (Ed.),
672 *Treatise on Geophysics* (2nd ed., Vol. 4, pp. 139–159). Elsevier. [https://doi.org/10.1016/B978-0-](https://doi.org/10.1016/B978-0-444-53802-4.00073-7)
673 [444-53802-4.00073-7](https://doi.org/10.1016/B978-0-444-53802-4.00073-7)

674 van den Ende, M. P. A., & Niemeijer, A. R. (2019). An investigation into the role of time-dependent
675 cohesion in interseismic fault restrengthening. *Scientific Reports*, *9*, 9894.
676 <https://doi.org/10.1038/s41598-019-46241-5>

677 Vidale, J. E., Ellsworth, W. L., Cole, A., & Marone, C. (1994). Variations in rupture process with
678 recurrence interval in a repeated small earthquake. *Nature*, *368*, 624–626.
679 <https://doi.org/10.1038/368624a0>

680 Vigil, G., Xu, Z., Steinberg, S., & Israelachvili, J. (1994). Interactions of silica surfaces. *Journal of*
681 *Colloid and Interface Science*, *165*, 367–385. <https://doi.org/10.1006/jcis.1994.1242>

682 Violay, M., Passelegue, F., Spagnuolo, E., Di Toro, G., & Cornelio, C. (2019). Effect of water and rock
683 composition on re-strengthening of cohesive faults during the deceleration phase of seismic slip
684 pulses. *Earth and Planetary Science Letters*, *522*, 55–64. <https://doi.org/10.1016/j.epsl.2019.06.027>

685 Wang, B., & Barbot, S. (2023). Pulse-like ruptures, seismic swarms, and tremorgenic slow-slip events
686 with thermally activated friction. *Earth and Planetary Science Letters*, *603*, 117983.
687 <https://doi.org/10.1016/j.epsl.2022.117983>

688 Xue, L., Li, H.-B., Brodsky, E. E., Xu, Z.-Q., Kano, Y., Wang, H., et al. (2013). Continuous permeability
689 measurements record healing inside the Wenchuan earthquake fault zone. *Science*, *340*(6140),

690 1555–1559. <https://doi.org/10.1126/science.1237237>

691 Yao, L., Shimamoto, T., Ma, S., Han, R., & Mizoguchi, K. (2013). Rapid postseismic strength recovery
692 of Pingxi fault gouge from the Longmenshan fault system: Experiments and implications for the
693 mechanisms of high-velocity weakening of faults. *Journal of Geophysical Research: Solid Earth*,
694 *118*, 4547–4563. <https://doi.org/10.1002/jgrb.50308>